Ultramicroscopy 220 (2021) 113162

Contents lists available at ScienceDirect

Ultramicroscopy

journal homepage: www.elsevier.com/locate/ultramic

Lattice resolution of vibrational modes in the electron microscope

Peter Rez *, Arunima Singh

Department of Physics, Arizona State University, Tempe, AZ 85287-1504, USA

ARTICLE INFO

Keywords:
Phonon
Lattice image
Silicon
Dynamical diffraction
Phonon dispersion

ABSTRACT

The combination of aberration correction and ultra high energy resolution with monochromators has made it possible to record images showing lattice resolution in phonon modes, both with a displaced collection aperture and more recently with an on –axis collection aperture. In practice the objective aperture has to include Bragg reflections that correspond to the observed lattice image spacings, and the specimen has to be sufficiently thick for adequate phonon scattered intensity. There has been controversy as to whether the images with the on axis detector are really a consequence of lattice resolution in a phonon mode or just a transfer of information from an image that was formed by elastically scattered electrons. We present results of calculations based on a theory that includes the possibility of dynamical electron diffraction for both incident and scattered electrons and the full phonon dispersion relation. We show that Umklapp scattering from the second Brillouin Zone back to the first Brillouin Zone is necessary for lattice resolution with the on axis detector and that it is therefore reasonable to attribute the lattice resolution to the phonon scattering.

1. Introduction

Phonons are the quantized oscillations of atoms in a crystalline solid. Electron beams can loose energy by exciting these modes, but can also gain energy from destroying phonons that are characteristic of thermal equilibrium at finite temperatures. Early work on phonon scattering in electron microscopy was concerned with its contribution to "anomalous absorption" and its effects on diffraction contrast [1,2]. There was also interest in how it gave rise to the diffuse background in diffraction patterns, and how the combination of phonon scattering and dynamical diffraction scattering led to the formation of Kikuchi lines and bands [3, 4]. The role of multi-phonon scattering, also known as thermal diffuse scattering, as the mechanism by which electrons were scattered to high angle annular dark field detectors led to renewed interest in theoretical formulation of phonon scattering in electron microscopy [5].

Recently electron microscopes have been equipped with a combination of energy loss spectrometers and monochromators that has made it possible to directly resolve phonon modes [6]. Originally only the higher energy optical modes, and the more complex phonon polariton modes characteristic of thin electron microscope specimens, were observed [7,8]. As the resolution of the spectrometer and monochromator improved, and the background from the tail of the zero loss peak was reduced, it became possible to detect acoustic modes, especially from flat regions of the phonon dispersion near Brillouin Zone boundaries where the energy was highest [9].

The combination of energy resolution sufficient to resolve a phonon mode and aberration correction that allows atomic column resolution, suggested that it should be possible to from an atomically resolved image in a phonon mode. Rez had predicted it should be possible to form lattice fringe image in an acoustic mode by selecting a scattering wave vector corresponding to a large Umklapp scattering perpendicular to a systematic line, giving rise to the fringe image [10].

Optic modes correspond to oscillating dipoles, hence the absorption of electromagnetic radiation. A consequence of the long-range nature of the electrostatic and magnetic interactions is that they can be excited with a distant electron beam, even outside the specimen. This can be used to advantage in damage free energy loss spectroscopy of beam sensitive organic specimens [11], but does seem to preclude atomically resolved images of optic phonon modes. The long range of the interaction means that the scattering is strongly forward peaked, the characteristic angle for a 200 meV loss is only 2 microrads for 60 keV electrons. It should therefore be possible to form a high-resolution image, provided the spectrometer or collection aperture does not overlap with the probe forming or objective aperture. This was demonstrated by Dwyer et al [12] who showed that nanometer resolution of the specimen edge was possible.

To achieve lattice resolution in STEM the probe-forming aperture should span a range of angles greater than the relevant Bragg angle [13].

* Corresponding author.
E-mail address: Peter.Rez@asu.edu (P. Rez).

https://doi.org/10.1016/j.ultramic.2020.113162
Received 8 May 2020; Received in revised form 28 October 2020; Accepted 1 November 2020
Available online 4 November 2020
0304-3991/

This is also the case for HAADF imaging. The collection aperture for the phonon scattered electrons is then displaced further from the optic axis, and the signal collection efficiency reduced. Nonetheless Hage et al [14] were able to demonstrate atomic resolution even through the collection apertures were displaced by 77 mrad.

Recently Venkatraman et al [15] demonstrated atomic resolution in both optic and acoustic modes in elemental Silicon with an on axis detector. Silicon is a special case, even though it has two atoms in each primitive cell, resulting in optic as well as acoustic modes, there is no charge transfer that gives rise to the oscillating dipole that potentially degrades spatial resolution. However it was argued that Venkatraman [15] did not really demonstrate lattice resolution in a phonon mode, the lattice resolution arose from interference among dynamically diffracted elastically scattered electrons. All the phonon did was transfer this information to the spectrometer. The same could be said for HAADF imaging, the resolution arises from the interference in the coherent electron probe, and the thermal diffuse scattering transfers the information to the detector while not degrading the spatial resolution. The recently demonstrated detection of localized modes associated with a single substituent atom of a different mass would suggest that atomic resolution in phonon modes is possible [16].

To disentangle all these effects a comprehensive theoretical model is needed that includes dynamical elastic scattering both before and after phonon scattering. To see which phonons contribute it is necessary that the model incorporate the full phonon dispersion relation. Many formulations of the theory for phonon scattering by electrons have been published [17–23], though not all have all the key ingredients. Our model, based on our earlier work [4,5], is described in the theory section. From calculations based on our model we show that the dominant contributions come from near the Brillouin Zone Boundaries. Large proportions of these regions are almost at a two-beam condition for 111 with a maximum intensity in the 111 beams. The interference that results in atomic resolution arises from the relatively large phonon Umklapp terms that direct intensity back into the on axis detector. It's therefore fair to say that the results of Venkatraman et al [15] really do represent imaging in a phonon mode and not an image from high resolution elastic scattering that happens to be directed to the spectrometer entrance aperture.

2. Theory

Most of the theory has been given before, in this section it is rewritten in a form suitable for calculating images in electrons scattered by phonons. Phonons are oscillations of the displacements of atoms in a crystal from their equilibrium positions. Since crystals are periodic phonons are Bloch functions and are uniquely defined by their polarization and their wave vector in the 1st Brillouin Zone. Each phonon has an energy which is related to the frequency, though it is possible for there to be degeneracies in frequency among modes in high symmetry directions. The frequencies are the eigenvalues and the displacements of the atoms in the unit cell are the eigenvectors of the dynamical matrix D. [25]

$$D\begin{pmatrix} k & \\ b & b' \\ \alpha & \alpha' \end{pmatrix} = \frac{e^{-i\mathbf{k}.\mathbf{R}_{b'}}}{M_{b'}}\phi\begin{pmatrix} k & \\ b & b' \\ \alpha & \alpha' \end{pmatrix}\frac{e^{i\mathbf{k}.\mathbf{R}_{b}}}{M_b} \tag{1}$$

where b labels atoms in the cell of mass M_b, α labels polarization and ϕ is the potential.

The number of modes is $3N$ where N is the number of atoms in the unit cell. Elemental semiconductors have 2 atoms in the primitive unit cell, so there are a total of 6 modes, 3 acoustic modes that have zero frequency at the Γ point, the Brillouin Zone center, and 3 optic modes that have finite frequency at the Γ point. In the experiments of Venkatraman et al [15] the crystal was oriented in the $1\bar{1}0$ orientation. For the range of scattering angles appropriate for 60 keV electrons it is only necessary to consider a single layer of reciprocal space. The main Bragg reflections are the 111, 220, and those related by symmetry. The phonon dispersion surfaces were calculated using Phonopy [26] from total energies calculated with VASP [27] for displacements of the two atoms in a

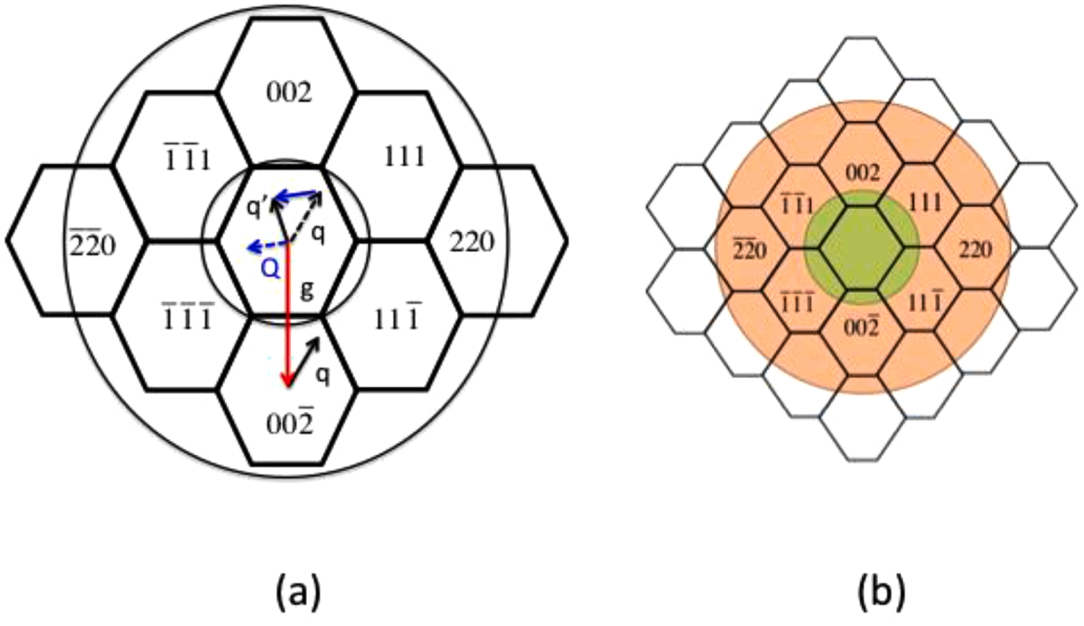

Fig. 1. (a) Diagram showing the geometry for phonon scattering. **q** denotes a point in a Brillouin Zone in the Objective aperture, **q'** a point in the Brillouin Zone of the spectrometer entrance aperture, in this case the first Brillouin Zone. To show the phonon wave vector **Q**, as the difference between **q'** and **q**, **q** is translated to the first Brillouin Zone and shown as a dashed line. Since the phonon dispersion relation is only defined in the 1st Brillouin Zone, **Q** has also been translated so that it starts at the Gamma point and is now shown as a dashed line. The reciprocal lattice vector for the initial wave vector $\mathbf{g} = 00\bar{2}$ is shown as a red line (b) Schematic diagram showing the incident probe and the detector angles in relation to the reciprocal lattice and the Brillouin Zones. The 28 mrad semi-angle incident probe is shown as the dark orange circle, the 12 mrad detector aperture is shown as the dark green circle and the 24 mrad detector aperture as the light green circle. From [15] Supplementary Information. (For interpretation of the references to color in this figure legend, the reader is referred to the web version of this article.).

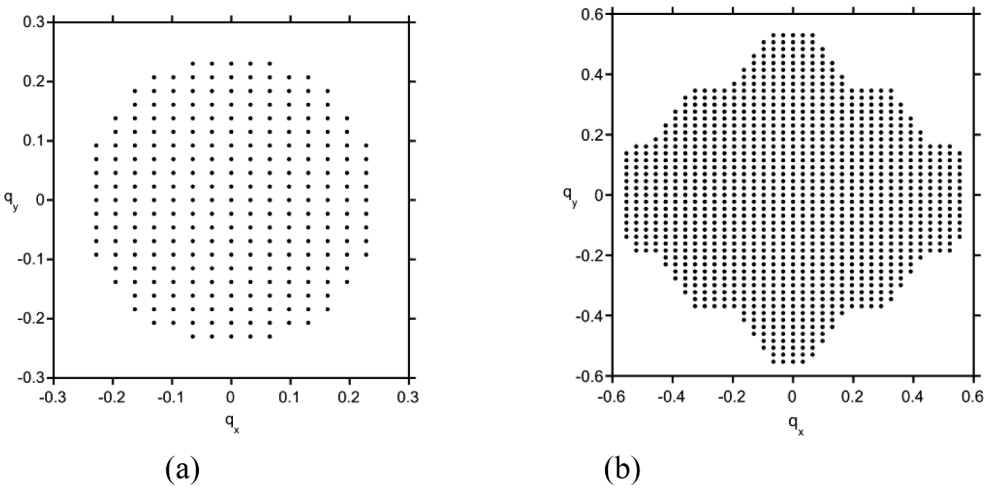

Fig. 2. Sampling the 12 mrad semi angle detector aperture (a) and the 28 mrad objective apertures (b).

4×4×4 supercell based on the primitive cell. The PAW potentials [28] and a grid of 5×5×5 k points were used in the VASP calculations.

The theory is very similar to that outlined by Amali and Rez [5] for HAADF imaging, later expanded on by Allen et al [29]. The phonon scattering amplitude, ψ , of electrons represented a plane waves can be derived by considering the structure factor for wave vector **s** and assuming that any displacements due to the phonons are small.

$$\psi(s) = \sum_b f_{el}^b exp(i\mathbf{s}.(\mathbf{R_b} + \mathbf{u_b})) \tag{2}$$

where f_{el}^b are electron scattering factors for atom b, $\mathbf{R_b}$ are the positions of atoms in the unit cell and $\mathbf{u_b}$ are phonon displacements. The phonon displacement term can be expanded as a 1st order perturbation.

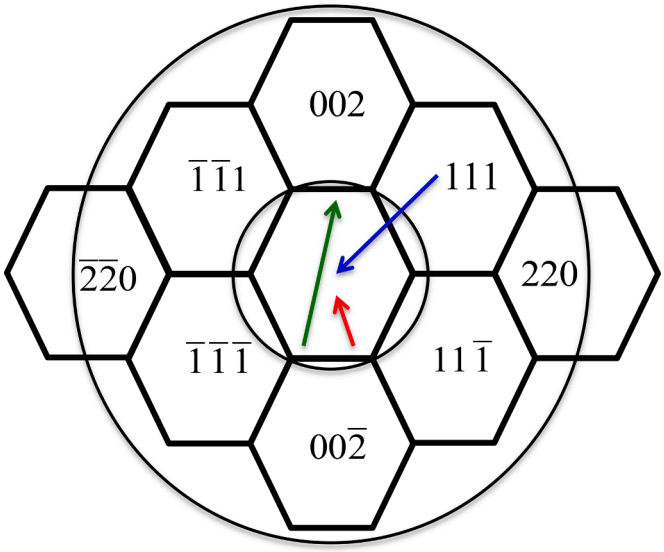

Fig. 3. Diagram showing 3 possible phonon wave vectors that connect reciprocal lattice vectors in the objective and detector apertures that are representative of Umklapp processes. The blue arrow clearly goes from the (111) Brillouin Zone to the (000) Brillouin Zone. To reduce the wave vector of the phonon shown as the green arrow to one quadrant of the first Brillouin Zone it is necessary to subtract a (111) reciprocal lattice vector. To place the phonon shown as the red arrow in the appropriate quadrant of the first Brillouin Zone a $(\bar{1}\bar{1}1)$ reciprocal lattice vector should be added. (For interpretation of the references to color in this figure legend, the reader is referred to the web version of this article.).

$$\psi(s) = \sum_b f_{el}\ (i\mathbf{s}.\mathbf{u_b}) exp(i\mathbf{s}.\mathbf{R_b}) \tag{3}$$

where we have dropped the index on the electron scattering factor as all the atoms in the cell are the same. Note that the scattering wave vector, **s**, has been partitioned between a component in the 1st Brillouin Zone, **Q** and a Bragg vector **g**, since the phonon wave vector is uniquely defined in the 1st Brillouin Zone.

This phonon scattering amplitude for plane wave electron states is expressed as an operator $H(\mathbf{Q}+\mathbf{g})$

$$H(\boldsymbol{Q}+\boldsymbol{g}) = (\boldsymbol{Q}+\boldsymbol{g}).\boldsymbol{e}\left(\frac{\hbar}{2M\omega(Q)}\right)^{\frac{1}{2}}\left(1+N\left(\frac{\hbar\omega}{k_BT}\right)\right)^{\frac{1}{2}} f_{el}(Q+g)(1+exp(i\boldsymbol{Q}.\boldsymbol{R})) \tag{4}$$

where $f_{el}(Q+g)$ is the electron scattering factor, $\boldsymbol{R}$ is the position of the 2nd atom in the primitive cell, M is the mass of the atom, $\omega(Q)$ is the frequency, $N\left(\frac{\hbar\omega}{k_BT}\right)$ is the Bose-Einstein occupation number and $\boldsymbol{e}$ is the polarization. Since in practice it is only possible to detect phonons with energies greater than k_BT in the electron microscope due to the background from the tail of the zero loss peak, $N\left(\frac{\hbar\omega}{k_BT}\right)$ is small, and it is only necessary to consider creation of phonons. For simplicity we will set it to zero, which is equivalent to assuming zero temperature. Creation of a phonon that results in scattering from one Brillouin Zone to another is called an Umklapp process. When the scattering is confined to a single

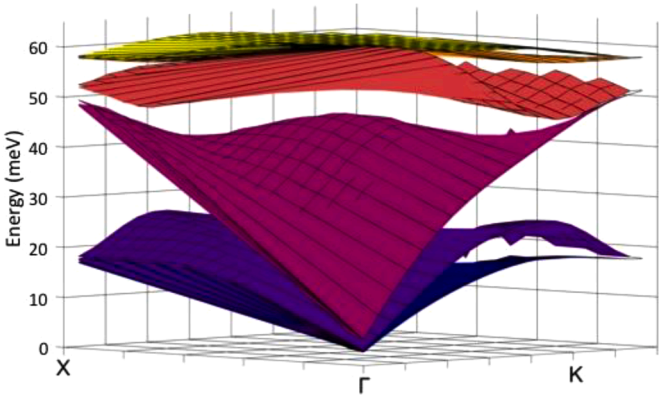

Fig. 4. 2D phonon dispersion surfaces for Si in the [110] projection (from [15] Supplementary Information).

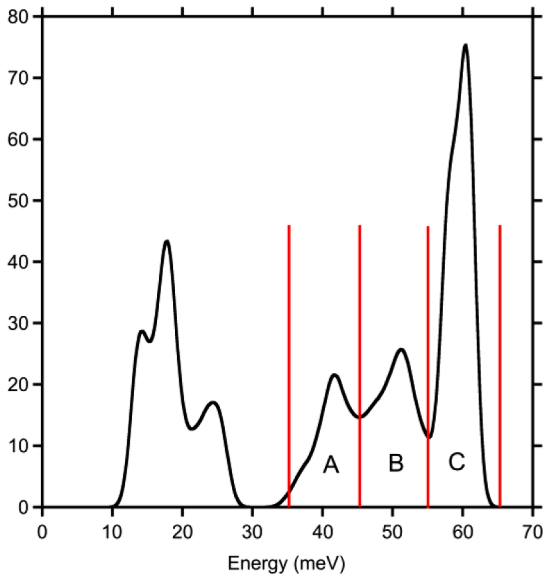

Fig. 5. Phonon density of states calculated from the 2D dispersion surfaces shown as Fig 4. Peak A between 35meV and 45 meV, Peak B between 45 meV and 55 meV and Peak C between 55 meV and 65 meV are shown.

Brillouin Zone it is called a Normal Process. As can be seen from the functional form of Eq. (4), plotted in Rez (2014) [24], Umklapp processes to the 2nd Brillouin Zone (in the case of 110 Silicon the Brillouin Zones around 111) dominate.

The electron source in a field emission microscope is sufficiently small and can be considered as a point emitting a spherical wave. The electron probe on the surface of the specimen can also be represented as a spherical wave defined by the range of angles allowed by the electron optics, that can be as great as 30 - 40 mrads semi angle with aberration correction. Since the corresponding wavevector in the plane of the specimen is greater than a reciprocal lattice vector it is possible to get lattice resolution from this coherent spherical wave as first shown by Spence and Cowley [13]. Specifying the incident probe wave vectors in the first Brillouin Zone by **q**, in a very thin specimen (a weak phase object) the scattered wave intensity to another position in the first Brillouin zone, **q'**, for a probe at position $\mathbf{r_p}$ would be

$$I(\mathbf{r_p}) = \sum_{L,L',g,g',h,h'} \int\int\int H(\mathbf{q}' - \mathbf{h} - \mathbf{q}) H^*(\mathbf{q}' - \mathbf{h}' - \mathbf{q}) \times A(\mathbf{q}+\mathbf{h}) A(\mathbf{q}+\mathbf{h}') \exp\left[-i(\mathbf{h}-\mathbf{h}')\mathbf{r_p}\right] d\mathbf{q}' d\mathbf{q}\, dz \quad (5)$$

where $\times A(\mathbf{q}+\mathbf{h})$ is 1 if that particular wave vector is allowed through the probe forming aperture, or zero otherwise. It could be modified by a phase shift from a wavefront aberration function, but we'll assume that we can neglect this phase shift for an aberration corrected microscope for the range of angles we are considering. The phonon wavevector, ***Q***, in the first Brillouin Zone is

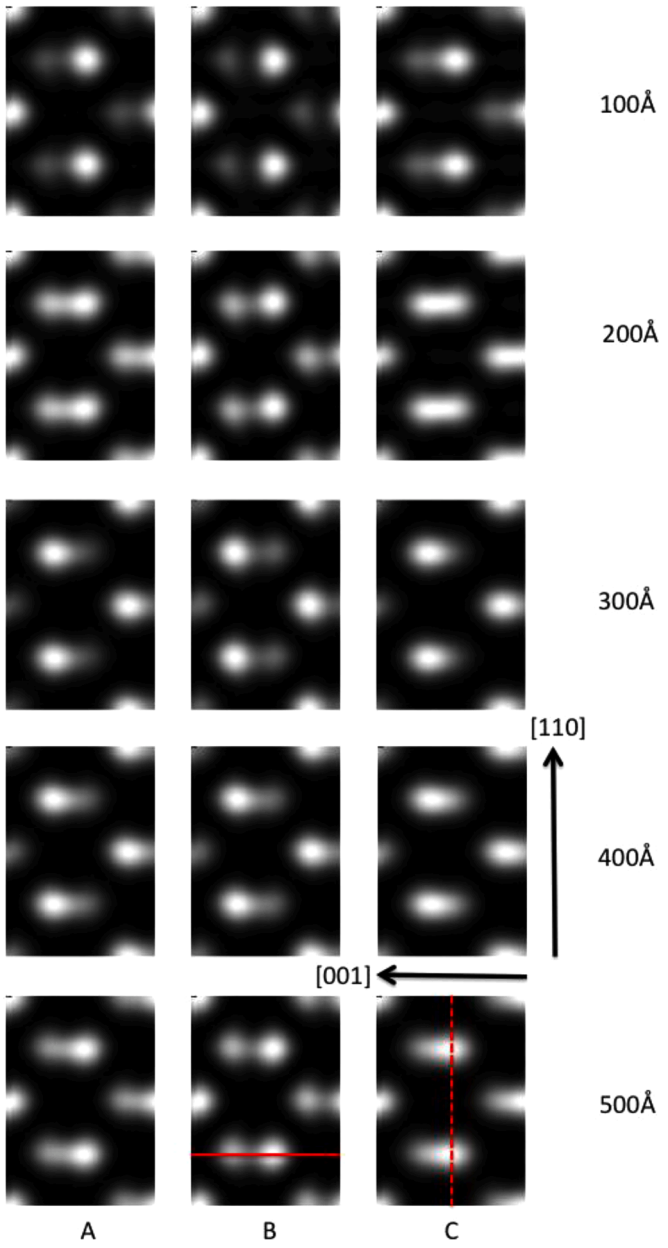

Fig. 7. Simulated images for Si [1$\bar{1}$0] for 60 keV electrons, objective aperture 28 mrad semi angle detector aperture 12 mrad. A,B, C correspond to selecting phonons with energies 35-45 meV, 45-55 meV, 55- 65 meV respectively as defined by the windows shown in Fig. 5. The solid red line shows the direction of the profile in Figs 8,10 and 12, the dashed red line is the direction of the profile in Figs 15 and 16. (For interpretation of the references to color in this figure legend, the reader is referred to the web version of this article.) .

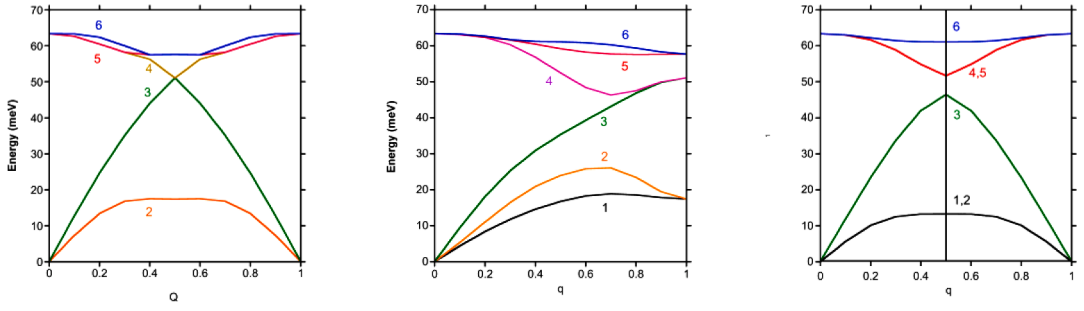

Fig. 6. Phonon dispersions along (a) (001) (b) (110) and (c) (111) showing the 3 acoustic and 3 optic modes.

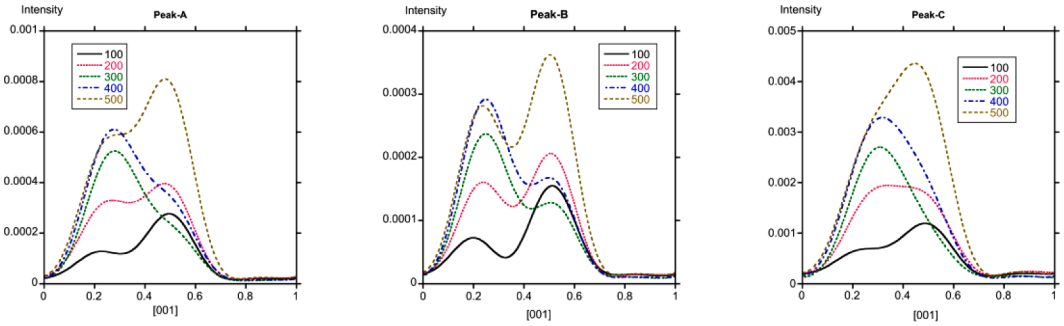

Fig. 8. Line profiles across dumb bells in the [001] direction for the images shown in Fig. 7.

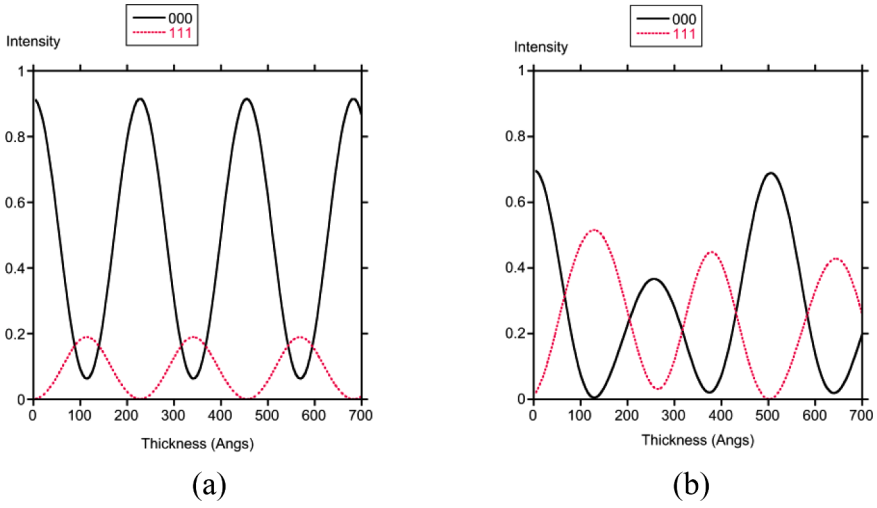

Fig. 9. Variation of elastically scattered intensity in the 000 and 111 beams with thickness due to dynamical diffraction for (a) the $[1\bar{1}0]$ zone axis and (b) tilted so that the (111) beam is at a 2 beam Bragg condition. The calculations used 9 beams and an accelerating voltage of 60 kV.

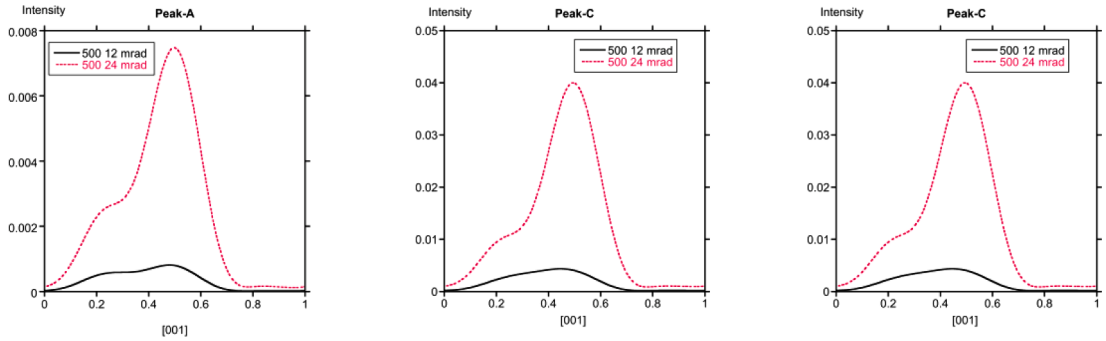

Fig. 10. Line profiles across dumb bells in the [001] direction for a thickness of 500 Å, with a 28 mrad semi angle objective aperture, and 24 mrad semi-angle detector aperture.

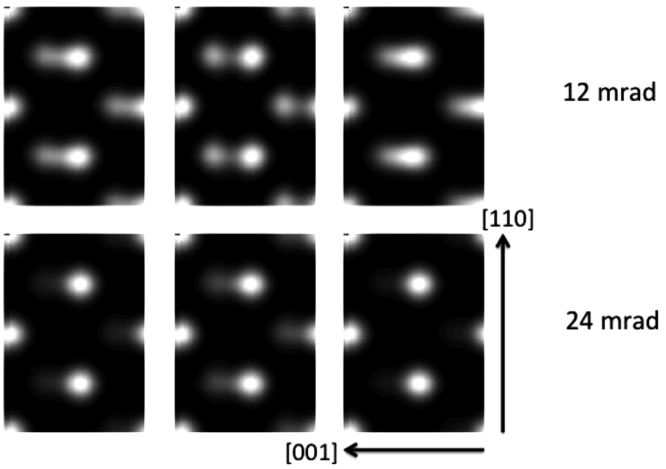

Fig. 11. Simulated images for a thickness of 500 Å, with a 28 mrad semi angle objective aperture, and 24 mrad semi-angle detector aperture.

$$\boldsymbol{Q} = \boldsymbol{q}' - \boldsymbol{q} \tag{6}$$

Electrons are scattered strongly in crystalline specimens and it is necessary to take account of dynamical diffraction, the multiple elastic scattering among diffracted beams. We should consider the dynamical diffraction among Bragg reflections for each wavevector in the 1st Brillouin Zone. For now we will represent the dynamical diffraction as a propagation operator

$P_{gh}(q,z)$ for the incident electron states, where g and h label Bragg reflections, q is a point in the 1st Brillouin Zone. In terms of the matrix of Bloch wave coefficients $C_{g,j}\ (q)$ and the eigenvalues $k_j(q)$ the propagation operator can be written as

$$P_{gh}(q,z) = \sum_j C_{g,j}(q) exp\left(ik_j(q)z\right) C^{-1}_{j,h}(q) \tag{7}$$

where g,h label beams and j labels the electron dispersion surface.

The corresponding operator for scattered electrons is $R_{gh}(q',z)$.

$$R_{gh}(q',z) = \sum_j C_{g,j}(q') exp\left(ik_j(q')z\right) C^{-1}_{j,h}(q') \tag{8}$$

Alternatively, the propagation operator can be calculated by the multislice method [30].

The phonon intensity when the probe is at position $\boldsymbol{r_p}$ is an integral over contributions from slices of thickness dz at depth z in a specimen of thickness t

$$\begin{aligned} I(\boldsymbol{r_p}) = & \sum_{M,M',L,L',g,g',h,h'} \int\int\int R_{ML}(\boldsymbol{q}',t-z) R^*_{M'L'}(\boldsymbol{q}',t-z) \\ & \times H(\boldsymbol{q}'+\boldsymbol{L}-\boldsymbol{g}-\boldsymbol{q}) H^*(\boldsymbol{q}'+\boldsymbol{L}'-\boldsymbol{g}'-\boldsymbol{q}) \\ & \times P_{gh}(\boldsymbol{q},z) P^*_{g'h'}(\boldsymbol{q},z)\ A(\boldsymbol{q}+\boldsymbol{h}) A(\boldsymbol{q}+\boldsymbol{h}') exp\left[-i(\boldsymbol{h}-\boldsymbol{h}')\boldsymbol{r_p}\right] d\boldsymbol{q}'\, d\boldsymbol{q}\ dz \end{aligned} \tag{9}$$

where **q'** represents the wavevector in the Brillouin Zone (BZ) characterizing the final state accepted by the spectrometer, **q** the wave vector in the BZ representing the initial state, **Q**= **q'-q** is the phonon wavevector L,L', g,g',h,h' are reciprocal lattice vectors. A schematic diagram showing the relationship between **q, q'** and **Q** for an Umklapp scattering to the $(00\bar{2})$ Brillouin Zone is given as Fig 1a.

3. Calculation procedure

The incident probe spans multiple Brillouin Zones as shown in Fig. 1b, the 12 mrad detector aperture is mainly in the 1st Brillouin Zone, while the 24 mrad detector also spans multiple Brillouin Zones. The most significant reciprocal lattice vectors are the 000 and set of 111 vectors, next in significance are 220 and 002, while the incident probe also overlaps the Brillouin Zone around 113 and 222 reciprocal lattice vectors.

Although Eq. (9) is a compact expression for the intensity it is not very convenient for computation as in a Bloch wave formalism it scales as N^8 where N is the number of beams. It is computationally more efficient to calculate the amplitudes generated by each phonon at each depth in the crystal, then store them in an array indexed by phonon responsible for the scattering, it's depth z and the reciprocal lattice vector specific to the incident beam, h.

$$\psi(h,q'-q,t,z) = \sum_{M,L,g} R_{ML}(q',t-z) H(q'+L-q-g) P_{gh}(q,z) A(q+h) \tag{10}$$

As originally shown by Young and Rez [31], and Gjonnes [32], summing over allowed phonon wave vectors perpendicular to the specimen results in a sum over contributions from different depths.

$$S(h,h') = \sum_{Q,z} \psi(h,Q,t,z) \psi^*(h',Q,t,z) \Delta z \tag{11}$$

The intensity for a probe position can then be calculated from

$$I(r_p) = \sum_{h,h'} S(h,h') exp\left(i(\mathbf{h}-\mathbf{h}').\mathbf{r_p}\right) \tag{12}$$

Even with this more efficient procedure there is a scaling of N^3 with number of beams, not to mention a matrix diagonalization that also scales as N^3. For this reason for calculations involving dynamical diffraction propagation only 9 beams, 000, the 111 set, the two 220;'s and the two 002's were used.

The first step is to evaluate the eigenvector matrices and eigenvalue vectors for all positions in the Brillouin Zone. The frequencies associated

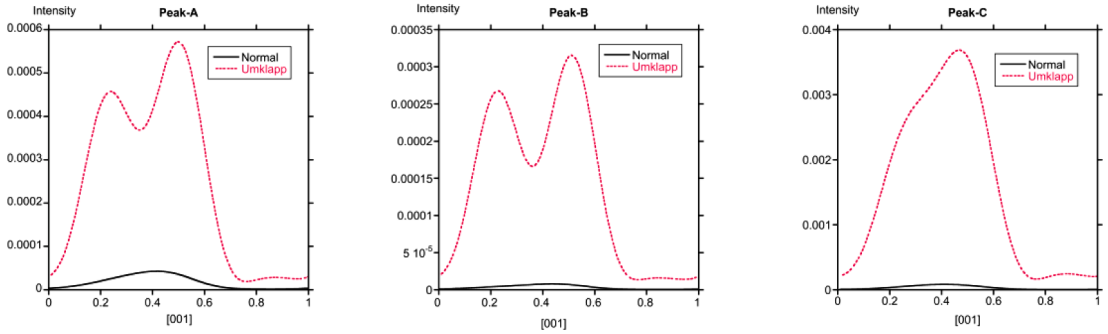

Fig. 12. Normal and Umklapp contributions to the profiles across the center of the dumbbell in the [001] direction for (a) Peak A (b) Peak B and (c) Peak C for a thickness of 500 Å and a 12 mrad semi angle detector angle.

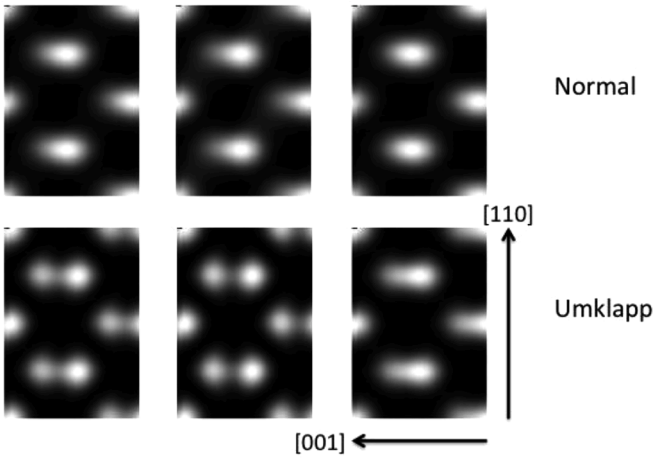

Fig. 13. Normal and Umklapp contributions to simulated images for (a) Peak A (b) Peak B and (c) Peak C for a thickness of 500 Å and a 12 mrad semi angle detector angle.

with each point were read in from the file generated by Phonopy [26]. These were only defined in one quadrant as the frequencies in the other quadrants are equivalent by symmetry. A grid with a spacing of 0.15 [001] was used, with 172 points in the 1st Brillouin Zone. This represented a reasonable compromise over adequate sampling and maintaining a clear separation between the different Brillouin Zones. Since the detector aperture is smaller than the objective aperture, the outer loop is over detector aperture reciprocal lattice vectors and the inner loop over the objective aperture positions. The grid of reciprocal lattice vectors spanning the 12 mrad aperture is shown as Fig. 2a and the grid for the objective aperture as Fig. 2b. Note the gaps in the objective aperture from the absence of the 311 and 222 reciprocal lattice vectors

Phonon wave vectors were calculated as the difference between a reciprocal lattice vectors in the objective aperture and the detector aperture. These were reduced to the first Brillouin Zone as shown in Fig. 3, since the frequency is only defined uniquely for reciprocal lattice vectors in one of the quadrants of the Brillouin Zone. At this stage modes with energies contributing to peaks identified from the phonon density of states could be selected. The matrix element given by Eq. (4) could then be calculated and from that the amplitudes Ψ. The advantage of this procedure is that a clear separation between Normal (**L-g**) =0 and Umklapp ($\mathbf{L}-\mathbf{g}$) $\neq 0$ could be made. Finally the matrix S, Eq. (11), was calculated with a loop over depths and phonon wave vectors. To match the experiments of Venkatraman et al [15] the electron accelerating voltage was set to 60 kV and a number of thicknesses up to 50 nm were calculated. A separate code was used to evaluate the intensity as a function of probe position, as a line profile with 100 points either parallel to [110] or [001] through the center of the dumb bells. Alternatively an image with 100 points along [001] and 141 points along [110] could be generated and viewed with Fiji [33]. A summary of the checks of the code is given in the Supplementary Information.

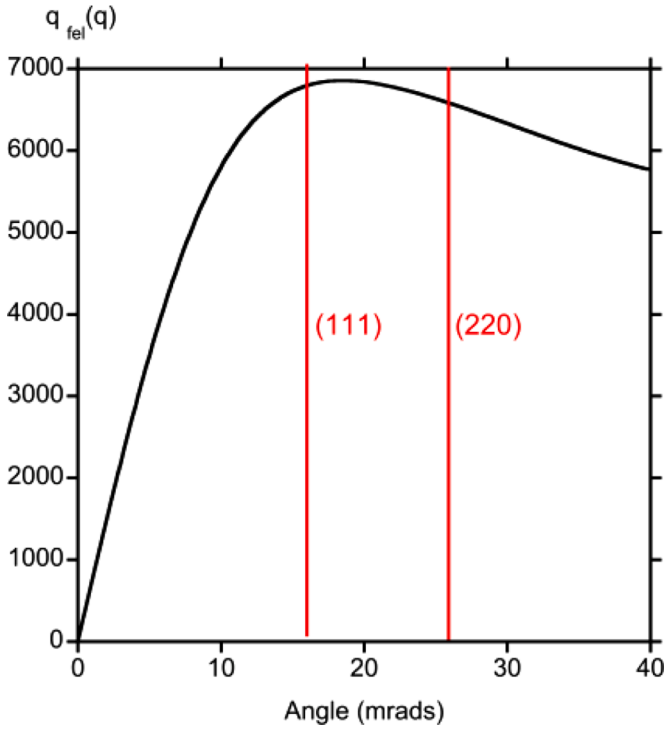

Fig. 14. Variation of $qf_{el}(q)$, as a function of scattering angle. Note how the maximum corresponds to the 111 reciprocal lattice vector.

An alternative strategy is to model the incident probe in a supercell. By definition creating a supercell means partitioning the Brillouin Zone into a grid. This probe is then propagated by the multislice algorithm to a given depth z. The phonon scattering operator is applied and the multislice algorithm used to propagate the phonon scattered wave to the exit surface. The procedure is almost identical to that shown as Eq. (10).

$$\psi(\mathbf{r_p},q,t,z) = \int R_{MS}(t-z)H(q)P_{MS}(z) * A(\mathbf{r_p}) \tag{11a}$$

where P_{MS} and R_{MS} denote multislice propagation for the incident and phonon scattered electrons and $H(q)$ is the phonon scattering for a wave vector q in the 1st Brillouin Zone and $A(\mathbf{r_p})$ is the probe function. The integral is over the detector aperture. The multislice propagation is efficiently performed by Fourier transform between a phase grating in real space and a propagator in reciprocal space [34]. The results are stored for each phonon wave vector in the Brillouin Zone and each depth and then summed according to Eq. (11). The advantage is that many more beams can be included, the disadvantage is the much higher cost in computer time. Effectively the propagation of elastic multiple scattering is recalculated for each phonon wave vector, and then everything has to be repeated for each of m probe positions. In this respect the procedure is very similar to the PRISM interpolation scheme of Ophus et al [35]. If there are n depths or slices then the calculation time will scale as

$$T \propto n \times N ln(N) \times m \tag{12a}$$

where N is the sampling of the supercell which could be as high as 1024^2. It would be best to implement this algorithm on a parallel computer. A further disadvantage is that it would be difficult to separate Normal from Umklapp terms.

4. Results

The 2D phonon dispersion surfaces are shown as Fig 4. A phonon density of states was calculated, shown as Fig. 5, from the 2D phonon dispersion surface of Fig. 4. Three peaks could be identified that were used to form images or line traces. Their origin could be determined from the dispersions along (001),(110) and (111) shown as Fig. 6.

The lowest energy peak, A, from 35-45 meV, only has a contribution from the longitudinal acoustic mode, branch 3. Peak B, from 45 meV to 55 meV, mainly comes from branch 4, one of the transverse optic modes, with about 1/3 the intensity from branch 3, the longitudinal acoustic mode. The highest energy peak, peak C, from 55 meV to 65 meV has approximately equal contributions from the three optic modes. Fig. 7 shows a tableau of calculated images in the three energy windows for thicknesses ranging from 100 Å to 500 Å. Line profiles through the peaks along [001] are shown as Fig. 8. Peak C from the optic modes has the highest intensity, which is to be expected as it has a higher density of states from modes with relatively flat dispersions across the Brillouin Zone. Peak B has very low intensity and was not observed in the

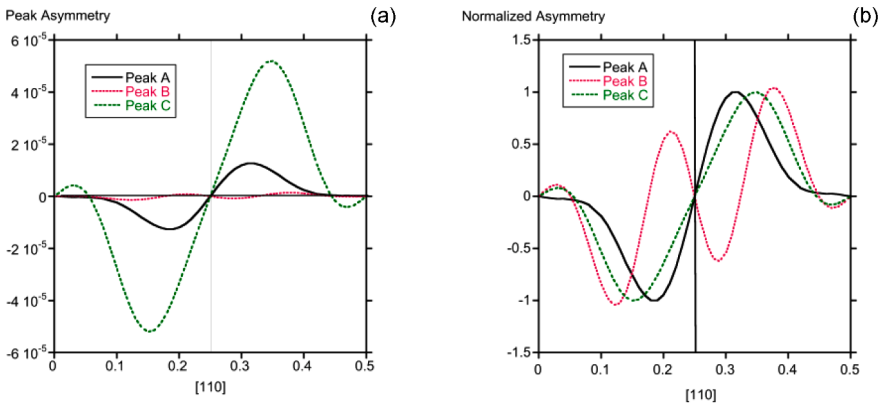

Fig. 15. (a) Plot of asymmetry in the profile of the dumb bell in the [110] direction for a thickness of 500 Å and a 12 mrad semi-angle detector aperture, (b) Asymmetry shown if (a) normalized to the maximum value.

experiment of Venkatraman et al [15]. The two peaks making up the dumb bell are resolved, though their relative intensity is sensitive to thickness. They are less distinct in the image formed from the higher energy optic phonon between 55 and 65 meV. This is no doubt because the intensity contributions from different phonons spanning most of the Brillouin zone are summed, whereas the lower energy acoustic mode image is dominated by phonons from near the Brillouin Zone boundary, as can be seen from Fig. 6. The sensitivity to thickness is not surprising given the strong dynamical diffraction. The images are dominated by the 000 and 111 beams, whose intensity variation with thickness for elastic scattering only is shown as Fig. 9 for both a zone axis condition and for the condition relevant for the 111 Brillouin Zone boundary, a 2 beam condition for 111. Repeating the calculation for more beams (13 beams including {113} set, and 17 beam including the {222} set) made no changes for the zone axis condition, but did alter relative intensities for the 111 Brillouin Zone boundary.

Increasing the detector (spectrometer) aperture to 24 mrad increased the phonon scattered intensity as shown for the calculated line profiles

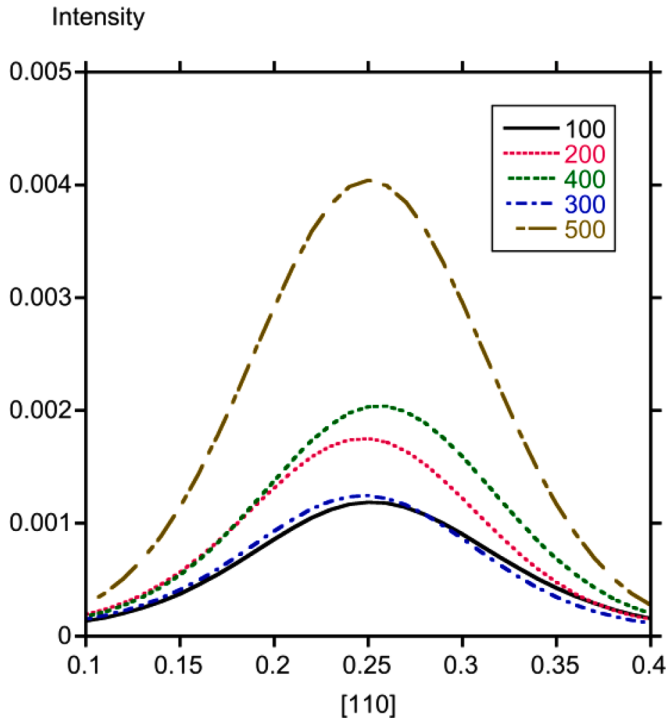

Fig. 16. Line profiles in the [110] direction across the center of the dumb bell at 0.25,0.25,0.5 for different thickness, for a 28 mrad semi-angle objective aperture and a 12 mrad semi-angle detector aperture.

along [001] for a thickness of 500 Å shown in Fig. 10. It also changed the relative intensity of the peaks in the dumb bell and only the peak at 0.25,0.25,0.5 is visible for the images simulated with the 24 mrad detector angle shown in Fig. 11. If elastic scattering alone were responsible for the contrast we would expect the contrast to be reduced when the collection aperture semi angle is increased to 24 mrad, almost the same as the objective aperture. Under these conditions practically the whole incident wavefunction would be collected and contrast could only arise from electrons scattered to much weaker higher order reflections.

The breakdown between Normal and Umklapp contributions was investigated by separately calculating their contributions in Eqs. (10)–(12) to images and profiles. Umklapp includes not only case where $L - g \neq 0$ but also those cases where a reciprocal lattice vector had to be added or subtracted so that the reduced phonon wave vector was in one of the quadrants of the first Brillouin Zone. Fig. 12 shows the contributions to each of the three peaks A, B and C. In all cases the Umklapp terms dominate. The Normal terms also do not show the splitting between the two peaks that make up the dumb bell as can be seen in the calculated image shown as Fig. 13.

The dominance of the Umklapp terms can be understood from a consideration of the form of the matrix elements, Eq. (4), and the variation of the intensity in each of the Bragg reflections. As can be seen from the dispersion relations shown as Figs. 4 and 6 the highest intensity for the lower energy peaks A and B comes from flat regions near the Brillouin Zone boundary. From Fig. 14 showing the form of the matrix element that goes as $qf_{el}(q)$, the intensity is at a maximum in the second Brillouin Zone. The dynamical scattering will only lead to an averaging over thickness. The form of the matrix element also explains the dominance of the signal in the 2nd Brillouin Zone for delocalized optic modes in hexagonal Boron Nitride observed by Senga et al [36] and Plotkin-Swing et al [37].

Venkatraman et al [15] observed shifts in peak positions in the [110] direction when a 12 mrad collection aperture was used. They hypothesized that this was due to a misalignment of the objective aperture. We repeated the calculation with a tilt of 2.6 mrad in the [110] direction. To ensure that no asymmetry was introduced into the objective aperture we also considered the {113} beams and added $(\overline{22}\ \overline{2})$ and $(\overline{222})$ beams. If the center of the peak at 0.25,0.25,0.5 is denoted as c, any asymmetry should be apparent from a plot of $I(c+x) - I(c-x)$ where x is the distance from c in the [110] direction. The plot is shown in Fig. 15a for a thickness of 500 Å. It would appear that the peak B shifts in the opposite direction to peaks A and C, best seen in the normalized intensity displayed as Fig. 15b. Since the magnitudes are of order 10^{-5} of the incident intensity the effect is far too small to account for the observations.

However line profiles in the [110] direction across the peak displayed as Fig. 16 showed apparent shifts with thickness. These shifts are still less than Venkatraman et al [15] observed. It is conceivable that the effect would be more significant if the calculations were repeated with

many more beams.

5. Conclusions

In scattering of high-energy electrons by phonons Umklapp scattering from the second Brillouin Zone back to the first Brillouin Zone dominates. Lattice resolution is possible when a coherent incident probe spans the reciprocal lattice vectors corresponding to lattice spacings in the image. To observe a lattice resolved phonon image with an on axis detector the calculations suggest that the specimen thickness must be enough to build up intensity in the diffracted beams. The Umklapp scattering then transfers intensity to the on-axis detector. Given that the Umklapp scattering is necessary for lattice resolution, and that the contrast increases with spectrometer collection angle, it is fair to say that the images observed by Venkatraman et al [15] are lattice resolved images in a phonon mode. The dynamical diffraction only serves to set up the conditions that make this possible.

Declaration of Competing Interest

The authors declare that they have no known competing financial interests or personal relationships that could have appeared to influence the work reported in this paper.

Acknowledgment

We would like to acknowledge discussions with K. Venkatraman, K. March, B.D. Levin, P.A. Crozier and funding from US National Science Foundation (grant no. CHE-1508667) is also acknowledged. The authors acknowledge the San Diego Supercomputer Center under the XSEDE Award No. TG-DMR150006 and Research Computing at Arizona State University for providing HPC resources.

Supplementary materials

Supplementary material associated with this article can be found, in the online version, at doi:10.1016/j.ultramic.2020.113162.

References

[1] H. Yoshioka, Effect of inelastic waves on electron diffraction, J. Phys. Soc. Jpn. 12 (1957) 618–627.
[2] C.R. Hall, P.B. Hirsch, Effect of thermal diffuse scattering on propagation of high energy electrons through crystals, Proc. R. Soc. A. 286 (1965) 158–177.
[3] S. Takagi, On the temperature diffuse scattering of electrons I. Derivation of general formulae, J. Phys. Soc. Jpn. 13 (1958) 278–297.
[4] P. Rez, C.J. Humphreys, M.J. Whelan, The distribution of intensity in electron diffraction patterns due to phonon scattering, Philos. Mag. 35 (1977) 81–96.
[5] A. Amali, P. Rez, Theory of lattice resolution in high angle annular dark field images, Microsc. Microanal. 3 (1997) 28–46.
[6] O.L. Krivanek, T.C. Lovejoy, N. Dellby, T. Aoki, R.W. Carpenter, P. Rez, E. Soignard, J.T. Zhu, P.E. Batson, M.J. Lagos, R.F. Egerton, P.A. Crozier, Vibrational spectroscopy in the electron microscope, Nature 514 (2014) 209–214.
[7] A.A. Govyadinov, A. Konecna, A. Chuvilin, S. Velez, I. Dolado, A.Y. Nikitin, S. Lopatin, F. Casanova, L. Hueso, J. Aizpurua, R. Hillenbrand, Probing low-energy hyperbolic polaritons in van der Waals crystals with an electron microscope, Nat. Commun. 8 (2017) 95.
[8] M.J. Lagos, A. Trugler, U. Hohenester, P.E. Batson, Mapping vibrational surface and bulk modes in a single nanocube, Nature 543 (2017) 529–532.
[9] F.S. Hage, R.J. Nicholls, J.R. Yates, D.G. McCulloch, T.C. Lovejoy, N. Dellby, O. Krivanek, K. Refson, Q. Ramasse, Nanoscale momentum-resolved vibrational spectroscopy, Sci. Adv. 4 (2018) eaar7495.
[10] P. Rez, Does phonon scattering give high resolution images ? Ultramicroscopy 52 (1993) 260–266.
[11] P. Rez, T. Aoki, K. March, D. Gur, O.L. Krivanek, N. Dellby, T.C. Lovejoy, S.G. Wolf, H. Cohen, Damage-free vibrational spectroscopy of biological materials in the electron microscope, Nat. Commun. 7 (2016) 10945.
[12] C. Dwyer, T. Aoki, P. Rez, S.L.Y. Chang, T.C. Lovejoy, O.L. Krivanek, Mapping vibrational modes with nanometer spatial resolution, Phys. Rev. Lett. 117 (2016), 256101.
[13] J.C.H. Spence, J.M. Cowley, Lattice imaging in STEM, Optik 50 (1978) 129–142.
[14] F. Hage, D.M. Kepaptsoglou, Q.M. Ramasse, L.J. Allen, Phonon spectroscopy at atomic resolution, Phys. Rev. Lett. 122 (2019), 016103.
[15] K. Venkatraman, B.D.A. Levin, K. March, P. Rez, P.A. Crozier, Vibrational spectroscopy at atomic resolution with electron impact scattering, Nat. Phys. 15 (2019) 1237–1241.
[16] F.S. Hage, G Radtke, D.M. Kepaptsoglou, M. Lazzeri, Q.M. Ramasse, Single-atom vibrational spectroscopy in the scanning transmission electron microscope, Science 367 (2020) 1124–1127.
[17] R.J. Nicholls, F.S. Hage, D.G. McCulloch, Q.M. Ramasse, K. Refson, J.R. Yates, Theory of momentum-resolved phonon spectroscopy in the electron microscope, Phys. Rev. B 99 (2019), 094105.
[18] C. Dwyer, Localization of high energy electron scattering from atomic vibrations, Phys. Rev. B 89 (2014), 054103.
[19] C. Dwyer, Prospects of spatial resolution in vibrational electron energy loss spectroscopy: implications of dipolar scattering, Phys. Rev. B 96 (2017), 224102.
[20] B.D. Forbes, A.V. Martin, S.D. Findlay, A.J. D'Alfonso, L.J. Allen, Quantum mechanical model for phonon excitation in electron diffraction and imaging using a Born–Oppenheimer approximation, Phys. Rev. B 82 (2010), 104103.
[21] B.D. Forbes, L.J. Allen, Modeling energy loss spectra due to phonon scattering, Phys. Rev. B 94 (2016), 014110.
[22] T. Niermann, Scattering of fast electrons by lattice vibrations, Phys. Rev. B 100 (2019), 144305.
[23] P.M. Zeiger, J. Rusz, Efficient and versatile model for vibrational STEM-EELS, Phys. Rev. Lett. 124 (2020), 025501.
[24] P. Rez, Is localized infrared spectroscopy now possible in the electron microscope? Microsc. Microanal. 20 (2014) 671–677.
[25] N.W. Ashcroft, N.D. Mermin, Solid State Physics, Harcourt Inc., Orlando, FL, 1976.
[26] A. Togo, I. Tanaka, First principles calculations in materials science, Scr. Mater. 108 (2015) 1–5.
[27] G. Kresse, J. Furthmuller, Efficient iterative schemes for ab initio total-energy calculations using a plane-wave basis set, Phys. Rev. B 54 (1996) 11169–11186.
[28] G. Kresse, D. Joubert, From ultrasoft pseudopotentials to the projector augmented wave method, Phys. Rev. B 59 (1999) 1758–1775.
[29] L.J. Allen, S.D. Findlay, M.P. Oxley, C.J. Rossouw, Lattice resolution contrast from a focussed probe. Part 1, Ultramicroscopy 96 (2003) 47–63.
[30] J.M. Cowley, Diffraction Physics, third ed., Elsevier, Amsterdam, 1995.
[31] A.P. Young, P. Rez, Resonance errors and partial coherence in the inelastic scattering of fast electrons by crystal excitations, J. Phys. C 8 (1975) L1–L7.
[32] J. Gjonnes, The influence of Bragg scattering on inelastic and other forms of diffuse scattering of electrons, Acta Cryst. 20 (1966) 240–249.
[33] J. Schindelin, I. Arganda-Carreras, E. Frise, Fiji: an open-source platform for biological image analysis, Nat.Methods 9 (2012) 1076–1079.
[34] K. Ishizuka, N. Uyeda, A New theoretical and practical approach to the multislice method, Acta Cryst. 33 (1977) 740–749.
[35] C. Ophus, J. Ciston, J. Pierce, T.R. Harvey, J. Chess, B.J. McMorran, C. Czarnik, H. H. Rose, P. Ercius, Efficient linear phase contrast in scanning transmission electron microscopy with matched illumination and detector interferometry, Nat. Commun. 7 (2016) 10719.
[36] R. Senga, K. Suenaga, P. Barone, S. Morishita, F. Mauri, T. Pichler, Position and momentum mapping of vibrations in graphene nanostructures, Nature 573 (2019) 247–250.
[37] B. Plotkin-Swing, G.J. Corbin, S. De Carlo, N. Delby, C. Hoermann, M.V. Hoffman, T.C. Lovejoy, C.E. Meyer, A. Mittelberger, R. Pantelic, L. Piazza, O. Krivanek, Hybrid pixel detector for electron energy loss spectroscopy, Utramicroscopy 217 (2020), 113067.